Experimental and Numerical Investigations of a Dual-Shaft Test Rig with Intershaft Bearing

M. Guskov, Jean-Jacques Sinou, Fabrice Thouverez, O.S. Naraikin

Hindawi Publishing Corporation
International Journal of Rotating Machinery
Volume 2007, Article ID 75762, 12 pages
doi:10.1155/2007/75762

Research Article

Experimental and Numerical Investigations of a Dual-Shaft Test Rig with Intershaft Bearing

M. Guskov,[1,2] J.-J. Sinou,[1,2] F. Thouverez,[1] and O. S. Naraikin[2]

[1] *Laboratoire de Tribologie et Dynamique des Systèmes, UMR CNRS 5513, Equipe dynamique des Structures et des Systèmes, Ecole Centrale de Lyon, 36 Avenue Guy de Collongue, 69134 Ecully Cedex, France*
[2] *Applied Mechanics Department, Bauman Moscow State Technical University, 2nd Baumanskaya Street, 5, Moscow 107005, Russia*

Received 26 June 2006; Revised 17 October 2006; Accepted 30 January 2007

Recommended by David P. Fleming

This paper deals with an experimental study of a dual rotor test rig. This machine, which was developed and built at the Laboratoire de Tribologie et Dynamique des Systèmes, Ecole Centrale de Lyon, will be first presented. It is composed of two coaxial shafts that are connected by an intershaft bearing and rotate independently, each one driven by its own motor. Their lateral vibrations and whirling motion are coupled by the intershaft bearing. The experimental tests consisting in run-ups and the associated measured unbalance response of the dual rotor will be investigated. The influence of the rotation of each rotor on the critical speeds and the associated amplitudes will be discussed. Moreover, this paper presents a numerical model of the dual rotor. Correlations between the experimental and numerical tests will be investigated. The objective is to be able to predict phenomena observed in experiments, starting from a rather fine numerical model.

1. INTRODUCTION

Because most of rotating machines operate in critical services in industries, the machines must operate with a high degree of reliability and the dynamic characteristics of turbomachinery need to be completely understood before a machine is placed in service [1–10].

Since the beginning of rotordynamic design, one of the objectives of researchers is to improve engine performance and to reduce operating costs. Indeed, the multiple-shaft rotating machinery has drastically increased and is quite a known design solution for power plant or propulsion organs. These machines represent a multiharmonic dynamical system and have quite a complex vibratory behavior. Some types of engines are characterized by a wide range of operational rotating speeds which requires an accurate prediction of critical speeds.

One of the ways to optimize the mass of the stator of multiple-shaft rotating machinery is the utilization of intershaft bearings. In 1975, Vance and Royal [11] has published an extensive discussion of the design and operational technological issues connected to the intershaft bearings. Hibner [12] has put forward the application of the transfer matrix method to the multiple-shaft machines in order to compute the critical speeds and nonlinearly damped response.

K. Gupta et al.[13] have presented a study on a counter-rotating dual Bently-Nevada-type rotor kit with an intershaft bearing. The system was modeled by a transfer matrix method in complex variables. The operational range of the rig includes one or two modes following the configuration. Cross-excitation phenomena have been encountered. Ferraris et al. [14] have analyzed in 1996 the rotordynamics of a prop-fan aircraft engine, which is a dual-shaft machine whose rotors spin at equal speeds in opposite directions with one eigenmode in the operational range. The finite element (FE) method, first developed by Nelson and McVaugh in 1976 [15], was used this time. A study of a twin-spool aircraft engine is also presented in the book of Lalanne and Ferraris [16]. A FE modal analysis is presented with a big number of various eigenmodes.

The current study is on a dual-shaft test rig that has been developed in order to study the dynamics of dual-rotor machines. The purpose of this paper is to present the experimental results compared to a numerical model for a case of corotation with a given constant spin speed ratio under residual unbalance. In the second part of the paper, a description of the experimental apparatus is given, comprising the

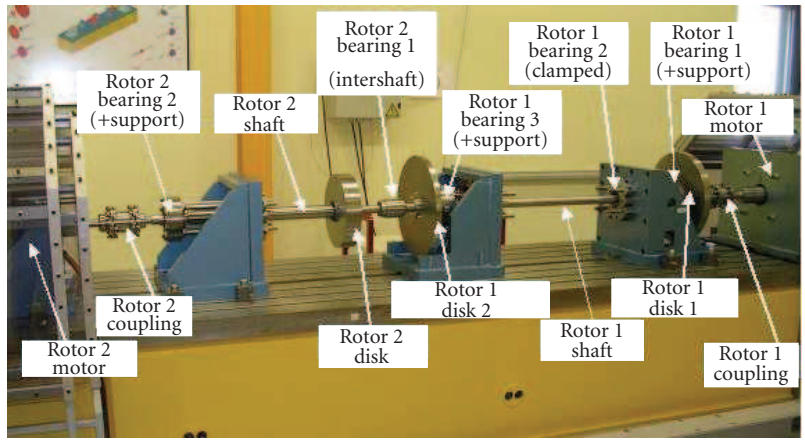

(a) Overall view

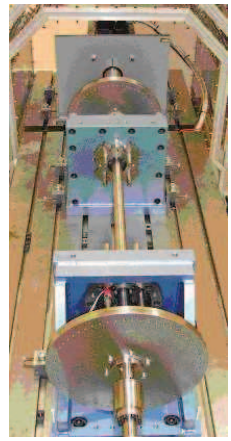

(b) Rotor 1

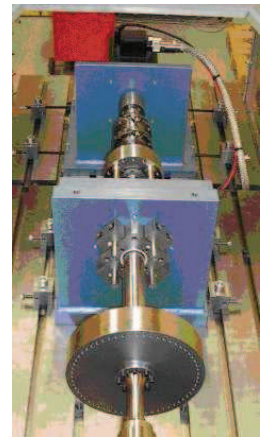

(c) Rotor 2

Figure 1: Dual-shaft test rig.

mechanical system and the measurement set. The linear FE model is presented in the next part. Finally, the experimental results of unbalance response are presented and compared with the FE model prediction results in order to evaluate the predictions by a detailed but rather basic numerical model. An improvement to the model is then proposed, consisting in taking into account the bearings tilting stiffness.

2. TEST RIG DESCRIPTION

2.1. *Mechanical system*

An overall view of the machine is given in Figure 1(a). The test rig consists of two shafts disposed along the same axis, connected by an intershaft bearing. The rotors are supported by five rolling element bearings. Three of the bearings are mounted in a compliant pedestal structure with adjustable stiffness, one is sealed in the pedestal and one bearing is intershaft. The intershaft bearing has one ring mounted on the shaft of rotor 1 and the other ring on rotor 2 as schematically shown on Figure 2. The rotor constitutive elements are shafts

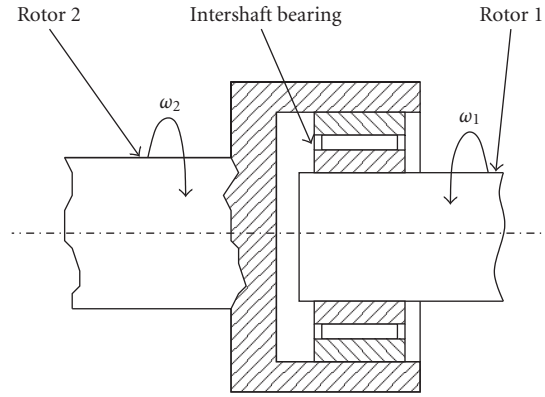

Figure 2: Intershaft bearing arrangement.

(circular section) and disks. Each of the shafts is driven by its own motor by means of flexible couplings, their spin speeds can therefore be different.

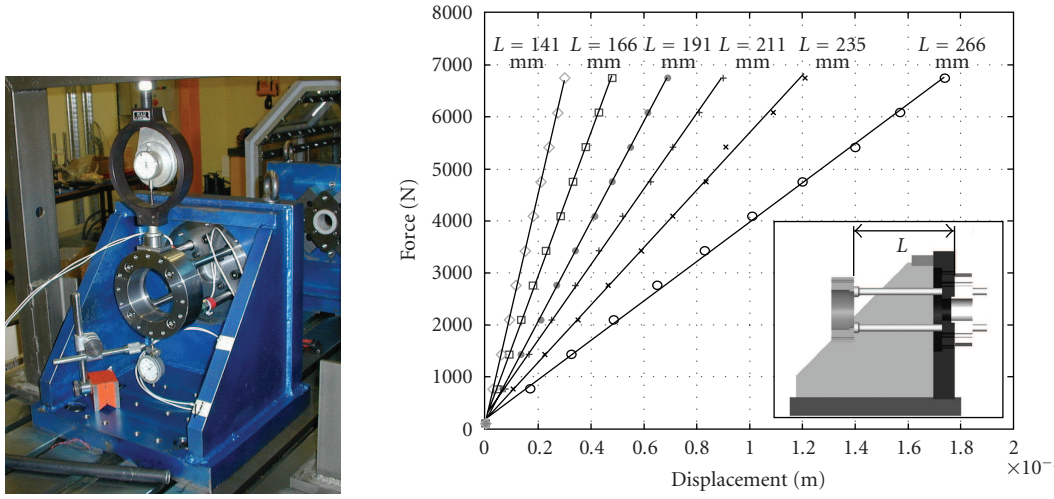

(a) Test setup

(b) Experimental characteristics

Figure 3: Static support compliance tests.

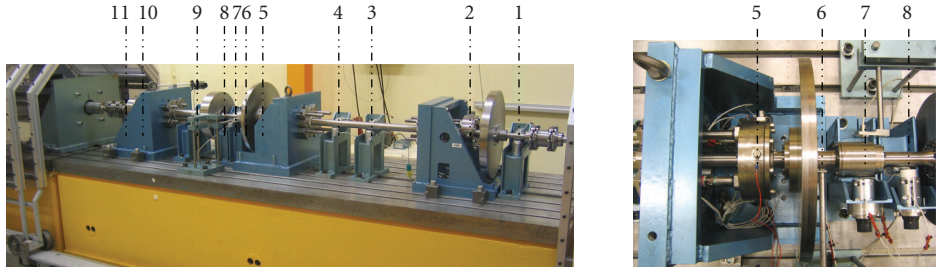

(a) Measurement stations

(b) Displacement measurement (stations 6, 7, and 8) and acceleration measurements (station 5)

Figure 4: Measurement instrumentation of the dual-shaft test rig.

The rotor 1 (Figure 1(b)) is 1.7 m long and has a mass of 100 kg. It comprises a 40 mm diameter shaft and two disks of 45 and 50 kg. It is carried on three bearings, two of which (bearings 1 and 3, Figure 1(a)) are mounted in compliant supports and one (bearing 2) is inset stiffly in the pedestal.

The rotor 2 (Figure 1(c)) is 1 m long and has a mass of 60 kg. It includes a variable cross-section shaft and a 40 kg disk. This rotor is borne by a bearing mounted in a flexible support and by rotor 1 by means of the intershaft bearing. The shaft includes a longer 60 mm diameter on the engine side part and a shorter 35 mm diameter one on the intershaft side.

The stiffness of compliant bearing supports is variable (see Figure 3) in order to keep one design solution for several supports with different characteristics. The horizontal rods length can be adjusted in order to obtain a required stiffness. A series of force-displacement tests has been effectuated so as to determine the actual length-stiffness function of the supports [10].

The test profiles are slow run-ups (5 rpm/s for rotor 2) through the range of the machine with the ratio of 2.8 between the two rotation speeds. The excitation is only due to the residual unbalance of the rotors.

The operational range of the machine is from 0 to 5500 rpm for each motor. In this study, rotor 2 is spinning 2.8 times faster than rotor 1. Because of the different rotation speeds, the critical speeds for each eigenfrequency occur twice, that is, when the value of this eigenfrequency coincides with the speed of the rotation of each rotor. That is why in what follows, for the critical speeds it will be noticed whether it occurs with respect to rotor 1 or 2.

2.2. Measurement instrumentation

Several types of measurements are realized. To assess the vibratory motion, displacements and the accelerations of the structure are measured in several transversal planes. The transducers used are eddy current probes for displacements and piezoaccelerometers for accelerations at each compliant support. (As seen on Figure 4, *rotor 1*: 1,3,4,6-eddy current probes; 2,5-bearing support accelerometers; *rotor 2*: 7,8,9,10-eddy current probes; 11-bearing support accelerometer.) The

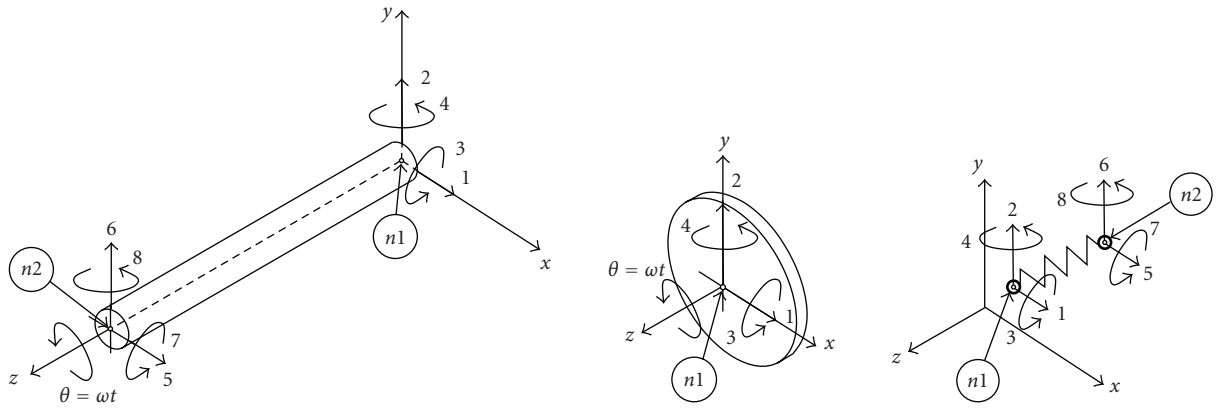

(a) Rod element (b) Disk element (c) Spring element

Figure 5: Finite elements used.

tachometry of the rotation is also recorded as well as a thermal monitoring of the bearing operational conditions. The measured vibratory data is transmitted to a PC via an HP VXI mainframe in the form of time history or order tracking. As indicated previously, two rotating speeds are present, and that is why the order tracking records are twice, that is, presented with respect to each rotor.

3. NUMERICAL COMPUTATIONS

3.1. Finite element model

The FE modeling of the machine is accomplished by means of Euler-Bernoulli rods (four degrees of freedom per node), present in the literature [2, 16] with the following assumptions:

(i) disks and supports inertia characteristics are modeled as lumped ones,
(ii) bearings, flexible supports, and rotor-motor couplings are modeled as two-node linear elastic spring elements,
(iii) damping is neglected for the eigenanalysis.

The finite elements used for this model (Figure 5) are formulated from the following equations of motion:

(i) rigid disks (four degrees of freedom, Figure 5(b)):

$$\mathbf{M}^d\ddot{\mathbf{x}}^d + \omega\mathbf{G}^d\dot{\mathbf{x}}^d = \mathbf{f}^d \tag{1}$$

with $\mathbf{M}^d$, $\omega\mathbf{G}^d$, ω, $\mathbf{x}^d$, $\mathbf{f}^d$ standing for the elementary mass matrix, the gyroscopic matrix, the spin speed, the nodal displacement vector, and external load vector,

(ii) shaft rod elements (eight degrees of freedom, Figure 5(a)):

$$\mathbf{M}^b\ddot{\mathbf{x}}^b + \omega\mathbf{G}^b\dot{\mathbf{x}}^b + \mathbf{K}^b\mathbf{x}^b = \mathbf{f}^b \tag{2}$$

with $\mathbf{M}^b$, $\omega\mathbf{G}^b$, $\mathbf{K}^b$, ω, $\mathbf{x}^b$, $\mathbf{f}^b$ standing for the elementary mass matrix, gyroscopic matrix, stiffness matrix, the spin speed, the nodal displacement vector, and external load vector,

(iii) springs (eight degrees of freedom, Figure 5(c)):

$$\mathbf{M}^s\ddot{\mathbf{x}}^s + \mathbf{K}^s\mathbf{x}^s = \mathbf{f}^s \tag{3}$$

with $\mathbf{M}^s$, $\mathbf{K}^s$, ω, $\mathbf{x}^s$, $\mathbf{f}^s$ standing for the elementary mass matrix, stiffness matrix, the spin speed, the nodal displacement vector, and external load vector.

After assembling, the general dynamics equations of the dual-rotor system may be written in the following form for each rotor:

$$\mathbf{M}_j\ddot{\mathbf{x}}_j + \omega_j\mathbf{G}_j\dot{\mathbf{x}}_j + \mathbf{K}_j\mathbf{x}_j = \mathbf{f}_j(t) + \mathbf{f}_{jg} - \mathbf{r}_j, \quad j = 1, 2, \tag{4}$$

where $\mathbf{M}_j$, $\mathbf{G}_j$, $\mathbf{K}_j$ are the mass, generalized damping, and stiffness global matrices of the system, $\mathbf{x}_j$, $\mathbf{f}_{jg}$, and $\mathbf{f}_j$ are the displacement, gravity load, and unbalance force vectors corresponding to the jth rotor. The vectors $\mathbf{r}_j$ represent the intershaft bearing reaction coupling terms between rotors.

Finally, we formulate the matricial dynamics equation of the whole system by replacing the intershaft bearing force vectors $\mathbf{r}_1$ and $\mathbf{r}_2$ by usage of the corresponding matrices:

$$\begin{bmatrix} \mathbf{M}_1^{11} & \mathbf{M}_1^{12} & 0 & 0 \\ \mathbf{M}_1^{21} & \mathbf{M}_1^{22} + \mathbf{M}_{\text{is}}^{11} & 0 & 0 \\ 0 & 0 & \mathbf{M}_2^{11} + \mathbf{M}_{\text{is}}^{22} & \mathbf{M}_1^{12} \\ 0 & 0 & \mathbf{M}_2^{21} & \mathbf{M}_2^{22} \end{bmatrix} \ddot{\mathbf{x}}_j + \omega_j \begin{bmatrix} \mathbf{G}_1^{11} & \mathbf{G}_1^{12} & 0 & 0 \\ \mathbf{G}_1^{21} & \mathbf{G}_1^{22} & 0 & 0 \\ 0 & 0 & \mathbf{G}_2^{11} & \mathbf{G}_1^{12} \\ 0 & 0 & \mathbf{G}_2^{21} & \mathbf{G}_2^{22} \end{bmatrix} \dot{\mathbf{x}}_j + \begin{bmatrix} \mathbf{K}_1^{11} & \mathbf{K}_1^{12} & 0 & 0 \\ \mathbf{K}_1^{21} & \mathbf{K}_1^{22} + \mathbf{K}_{\text{is}}^{11} & \mathbf{K}_{\text{is}}^{12} & 0 \\ 0 & \mathbf{K}_{\text{is}}^{21} & \mathbf{K}_2^{11} + \mathbf{K}_{\text{is}}^{22} & \mathbf{K}_1^{12} \\ 0 & 0 & \mathbf{K}_2^{21} & \mathbf{K}_2^{22} \end{bmatrix} \mathbf{x}_j = \begin{bmatrix} \mathbf{f}_1^1(t) + \mathbf{f}_{1g}^1 \\ \mathbf{f}_1^2(t) + \mathbf{f}_{1g}^2 \\ \mathbf{f}_2^1(t) + \mathbf{f}_{2g}^1 \\ \mathbf{f}_2^2(t) + \mathbf{f}_{2g}^2 \end{bmatrix}. \tag{5}$$

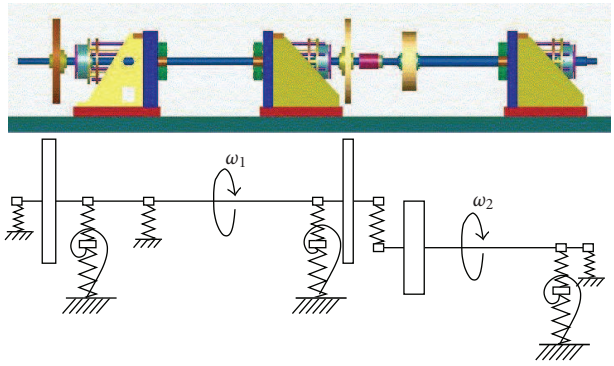

Figure 6: FE model.

Here the superscripts 1 and 2 reflect the splitting of the rotor matrices into coupled and uncoupled parts while the subscript "is" indicates the intershaft bearing matrices. The current study considers an undamped system model of 516 degrees of freedom, involving 129 nodes, see Figure 6.

For this study, the residual unbalance distribution is unknown. Assuming the operation of the system is steady, it can be stated that the forcing terms are composed of two harmonic components of the synchronous excitation due to unbalance and the static component due to the gravity. The expression of unbalance force vectors is expressed by the next equation:

$$\mathbf{f} = \omega_j^2 \mathbf{f}_{0j} e^{\mathbf{i}\omega_j t}, \quad j = 1, 2, \ \mathbf{i} = \sqrt{-1}, \tag{6}$$

where $\mathbf{f}_{01}$, $\mathbf{f}_{02}$ are constant vectors.

3.2. Eigensolution

The main analysis problems posed for this model are two types of eigenproblems—Campbell diagram construction as well as critical speeds research. The generalized damping matrix is then given by the gyroscopic matrix that is a sum of two matrices constructed for each rotor:

$$\mathbf{G} = \omega_1 (\mathbf{G}_1 + \eta \mathbf{G}_2) \quad \text{with } \eta = \frac{\omega_2}{\omega_1}, \tag{7}$$

with ω_i rotation speed of the ith rotor ($i = 1, 2$). η defines the ratio between the rotation speeds of the two rotors. As mentioned before, in this study $\eta = 2.8$. The Campbell diagram is the chart showing the eigenfrequencies evolution with the rotating speed of the studied system. The associated complex eigenproblem is

$$(\lambda^2 \mathbf{M} + \lambda \omega_1 (\mathbf{G}_1 + \eta \mathbf{G}_2) + \mathbf{K})\mathbf{x} = 0. \tag{8}$$

Here λ stands for the researched eigenvalues and associated eigenvectors, $\mathbf{x}$ is the rotation speed of rotor 1. The computed Campbell diagram is given on Figure 7. The dashed and dashed-dotted lines show the frequency of synchronous (order 1) excitation with rotor 1 and rotor 2, respectively. Bold and thin solid lines denote the forward ("stiffening") and backward ("softening") whirl modes evolution, respectively. The intersection of the synchronous excitation lines

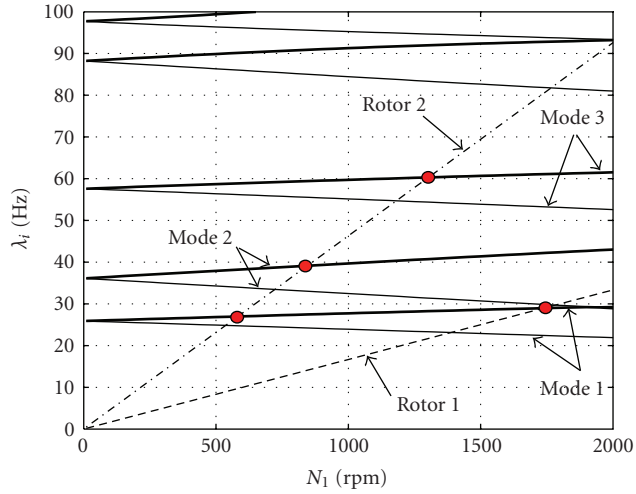

Figure 7: Computed Campbell diagram.

Table 1: Critical speeds with respect to rotor 1.

Rotating speed N_1 (rpm)	*Rotating speed N_2 (rpm)*
1388	3855
1738	4829
1783	4952

with the eigenmode lines gives place to critical speeds. On Figure 7, the critical speeds for forward modes are given by the bold dots. As the rotordynamical system model is axisymmetrical, only the forward modes are supposed to respond to the unbalance excitation.

Critical speeds may be sought by equating in (8) one of the rotation speeds of the rotors to an eigenfrequency:

$$\lambda = \mathbf{i}\omega_1 \tag{9}$$

for rotor 1 unbalance, and

$$\lambda = \mathbf{i}\omega_2 = \eta \mathbf{i}\omega_1 \tag{10}$$

for rotor 2 unbalance. We have then two eigenproblems:

$$\begin{aligned} &(\lambda^2 (\mathbf{M} + (\mathbf{G}_1 + \eta \mathbf{G}_2)) + \mathbf{K})\mathbf{x} = 0, \\ &\left(\lambda^2 \left(\mathbf{M} + \left(\frac{1}{\eta}\mathbf{G}_1 + \mathbf{G}_2\right)\right) + \mathbf{K}\right)\mathbf{x} = 0 \end{aligned} \tag{11}$$

which yield critical speeds and the associated modal shapes with respect to the speed of each rotor.

The resulting values of critical speeds are given alongside with the deviation from the experimental results (order-one response with respect to the corresponding rotor) in Table 1 (rotor 1) and Table 2 (rotor 2). It should be noticed that the modes at 1388 and 1783 rpm (rotor 1) from Table 1 as well as 537, 723, 1181 rpm (rotor 2) from Table 2 are backward whirl ones. This can be seen on the Campbell diagram (Figure 7, these frequencies occur on intersections of the synchronous excitation and decreasing branches of eigenfrequencies evolution).

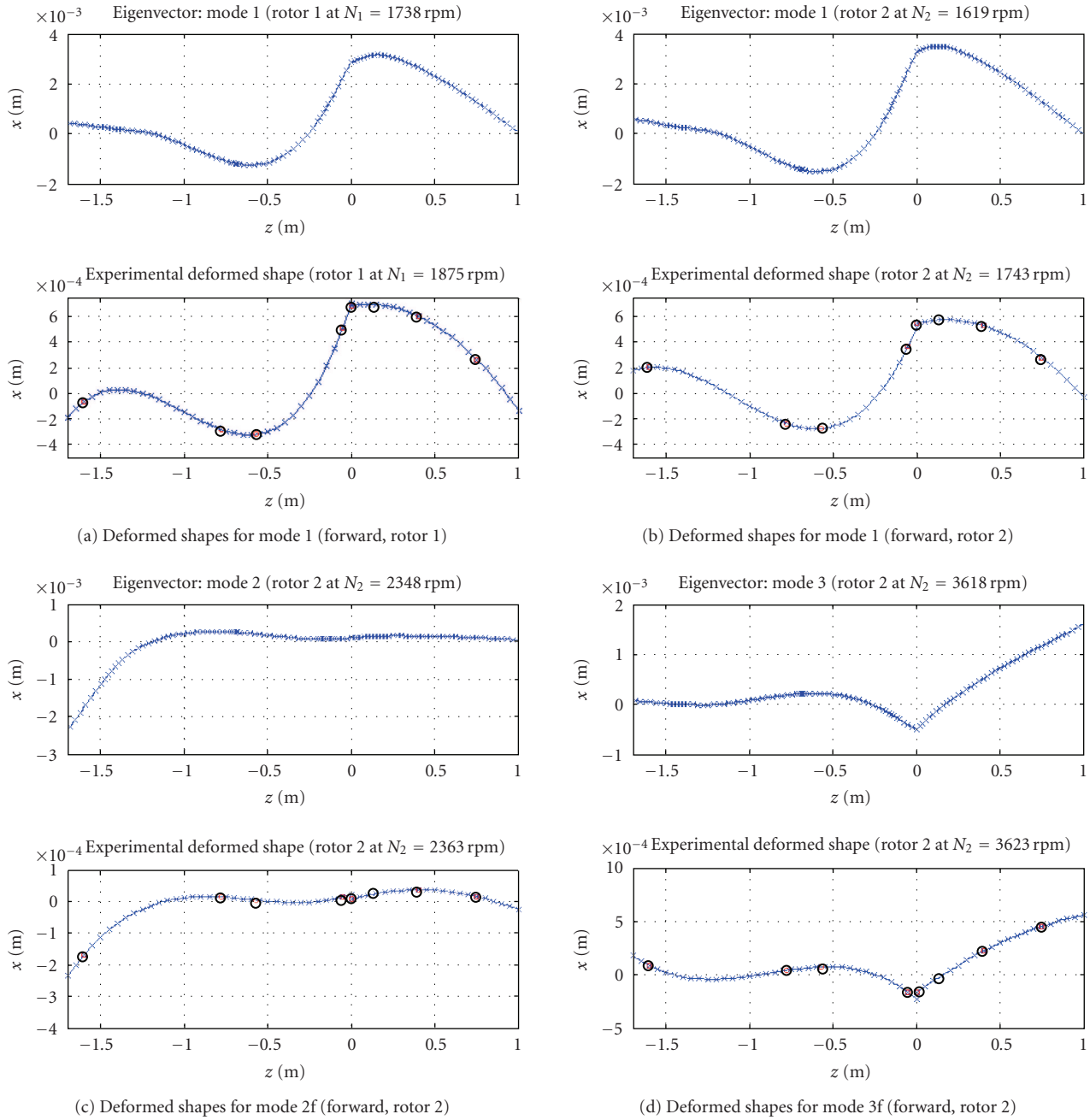

(a) Deformed shapes for mode 1 (forward, rotor 1)

(b) Deformed shapes for mode 1 (forward, rotor 2)

(c) Deformed shapes for mode 2f (forward, rotor 2)

(d) Deformed shapes for mode 3f (forward, rotor 2)

Figure 8: Deformed shapes: predicted (upper) and observed (lower). Bold dots denote measurement stations.

The rotordynamics eigenmodes associated with these critical speeds are shown on Figure 8 alongside with the operational deformed shapes. These mode shapes are given only for the forward modes (bold points on Figure 7), while the backward ones are quite similar.

4. EXPERIMENTAL RESULTS

4.1. Time history

The time history records represent the crude data on the experience. As previously explained, the test profiles are slow run-ups (5 rpm/s for rotor 2) in the range of the machine with the ratio of 2.8 between the two rotation speeds, as shown on Figure 9, and the excitation is realized by the residual unbalance of the rotors.

As may be seen in Figure 9, the first part of the record ($t < 1050$ s) corresponds to the slow run-up while the rest of the test time span ($t > 1050$ s) stands for the faster run-down. The unbalance response plots (see Figure 10) have therefore a characteristic pattern: the shape of the response envelope of the run-up segment can be recognized in the run-down as a deformed reflection in a mirror. Generally, the magnitude

Table 2: Critical speeds with respect to rotor 2.

Rotating speed N_1 (rpm)	*Rotating speed N_2 (rpm)*
537	1490
583	1619
723	2008
845	2348
1181	3282
1303	3618
1766	4905

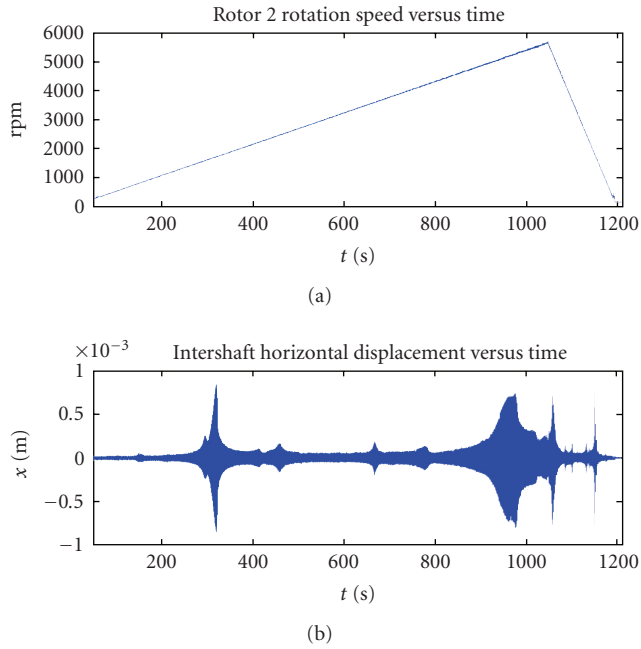

Figure 9: Test schedule.

of the peaks is lower on the run-down part, because the intense vibrations have not enough time to settle. In spite of this slender difference, the frequency position of the peaks is maintained, which justifies the quasisteady modeling, implied in Section 3.1.

One may see a number of peaks passed during the test. The most significant peaks correspond to the forward whirl frequencies of eigenmodes. It should be remarked also that the frequency range of the maximum response magnitude is not the same for all the probes: the antinodes of each mode shape are situated differently.

4.2. Order tracking and deformed shapes

Order tracking is a DSP method of filtering the measured time history signal so as to access its harmonic contents.

Some of the order tracking plots are presented in Figures 11 and 12: composite power (the whole signal magnitude, "CP" line), orders 1 and 2 with respect to each rotor. The composite power plot repeats the envelope of the time history plot. Considering the filtered order response plots allows us a deeper insight in the behavior of the rig.

The order 1 response peaks correspond to the critical speeds. As we can see, the backwhirl modes' response is present, although smaller than the forward one. This might be due to dissymmetries occurring in rolling element bearings with clearance under gravity load. Imperfections of the symmetry can be stated because of the difference between horizontal and vertical measured responses: horizontal displacements are slightly bigger than vertical ones and a characteristic response orbit rotation occurs near backward criticals, see Figure 13. Mode 1 (Figures 8(a), 8(b)) response is of greater magnitude around the intershaft bearing station (Figure 11(c) rotor 1, or Figure 12(c) rotor 2). This mode is the only one excited by both rotors in the operational range of the rig. The peak of the response to the rotor 2 unbalance is visibly sharper than the peak of the response to the rotor 1 unbalance. This is caused by the difference of the angular acceleration of the two rotors. Mode 2 (Figure 8(c)) brings about strong vibrations on the motor end of rotor 1 (Figure 12(a)). Rotor 2 has relatively low amplitudes on the second modal shape, that is why the backward whirl of this mode is not seen on the rotor 2 response. As for the rotor 1 response, the unbalance on this mode is quite big, as can be seen from Figure 11(a): even far from resonance peaks, the vibratory level is high which might be caused by a shaft bow, a misalignment rather than by a strong unbalance on disk 1. However, as can be seen from the Campbell diagram (Figure 7) for rotor 1, its backward whirl critical speed is close to the forward one of mode 1, and its response is eclipsed by the latter. Mode 3 response to rotor 2 unbalance can be fairly observed on most of the rig, especially on its opposite end (see, e.g., Figure 12(d)).

Besides the linear predictions, we note that the order 1 response is not enough to explain all the peaks of the vibration. The order 2 peaks (as compared to order 1, primary peaks) occur at speed approximately half of the respective primary peaks; this is perfectly in accordance with the Campbell diagram. The data on the experimental observation is summarized in Table 3. The causes of the 2X response might include misalignment, or imperfections of rotor axial symmetry, as suggested by [2, 5], and require nonlinear modeling.

Finally, the operational deformed shapes are given on Figure 8 alongside with the theoretical finite element predictions. It should be noticed that in spite of the discrepancies on the critical speed values, the operational deformed shapes are in a qualitative agreement with the numerical ones. It should be remarked also that although a strong resemblance is observed on Figure 8, the operational deformed shapes are not exactly the modal shapes, but result from the response of the system to the residual unbalance excitation. However, their consideration enables to ensure a better critical speed recognition.

4.3. Model improvement

The discrepancies between the analytical critical speeds and the experimental ones might be brought about by insufficient

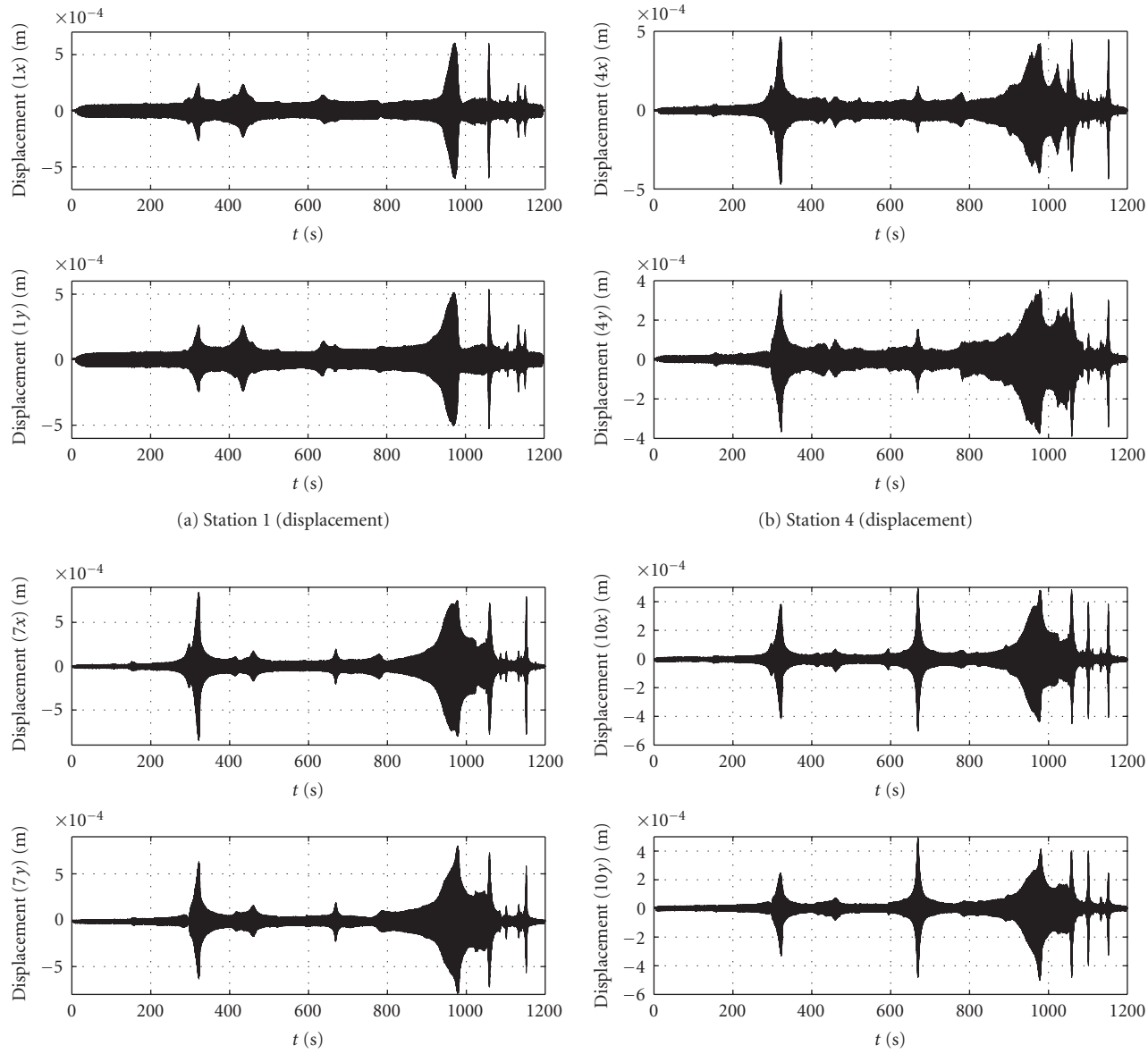

(a) Station 1 (displacement)

(b) Station 4 (displacement)

(c) Station 7 (displacement)

(d) Station 10 (displacement)

Figure 10: Time history measurements (stations 1, 4, 7, and 10).

modeling of some components of the rig. Specifically, lack of detailed information takes place for bearings and flexible couplings. By experience from previous studies of similar scale test rigs, as stated by Sinou et al. [10], the tilting compliance of bearings, usually omitted in rotordynamical models, may have a nonnegligible effect on the critical speed. A research of tilting stiffness is undertaken in order to minimize the overall quadratic error on the disposable critical speeds data (Figure 14), by investigating two parameters of the model previously set to zero—tilting stiffness k_{balls} of ball bearings and k_{rollers} of roller bearings. Thereby, the correlations between the numerical and experimental tests and the determination of the tilting stiffness k_{balls} of ball bearings and k_{rollers} of roller bearings are undertaken by considering the minimization of the following relation:

$$R^{\text{quad}} = \sqrt{\sum_i r^{\text{quad}^2}_{\text{rotor 1},i} + \sum_i r^{\text{quad}^2}_{\text{rotor 2},i}}, \tag{12}$$

with

$$r^{\text{quad}}_{\text{rotor 1},i} = \frac{\left| \nu^{\text{exp}}_{\text{rotor 1},i} - \nu^{\text{th}}_{\text{rotor 1},i} \right|^2}{\nu^{\text{exp}^2}_{\text{rotor 1},i}};$$
$$r^{\text{quad}}_{\text{rotor 2},i} = \frac{\left| \nu^{\text{exp}}_{\text{rotor 2},i} - \nu^{\text{th}}_{\text{rotor 2},i} \right|^2}{\nu^{\text{exp}^2}_{\text{rotor 2},i}}; \tag{13}$$

where $\nu^{\text{th}}_{\text{rotor 1},i}$ and $\nu^{\text{th}}_{\text{rotor 2},i}$ are the numerical resonant frequencies of the system at rest for the backward and forward

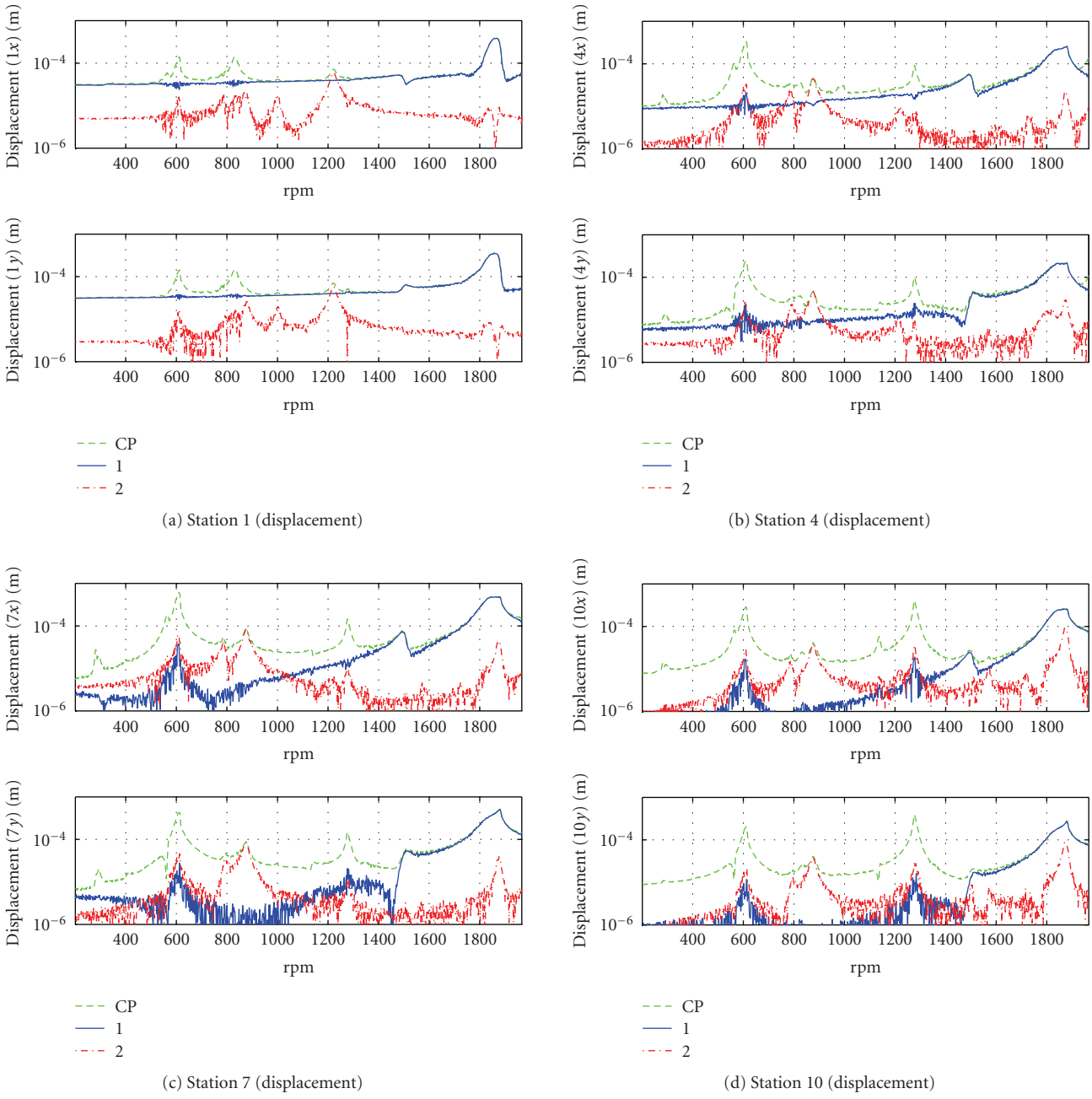

FIGURE 11: Order tracking measurements (rotor 1 reference, stations 1, 4, 7, and 10).

modes for rotors 1 and 2, respectively. $\nu^{\text{exp}}_{\text{rotor 1},i}$ and $\nu^{\text{exp}}_{\text{rotor 2},i}$ are the experimental estimated resonant frequencies of the system at rest for the backward and forward modes for rotors 1 and 2, respectively.

The minimum of the quadratic error, initially situated at 15%, is found for $k_{\text{balls}} = 3700\,\text{Nm/rad}$ and $k_{\text{rollers}} = 700\,\text{Nm/rad}$, at 9%.

5. CONCLUSION

This research presented a test rig dedicated to the study of coaxial dual rotors. By both experimental and numerical approaches, the test rig had its dynamics described in detail. Secondly, the presented linear model, used for the design of the discussed test rig, has yielded results that are in good agreement with the experimentally observed situation. The modal situation is therefore satisfactory as compared to the one required initially. However, the experimental values of critical speeds are systematically higher than the theoretical ones. An improvement to the rolling bearing model is made by including the tilting stiffness. The presence of the superharmonic response of order 2 is also to be noticed.

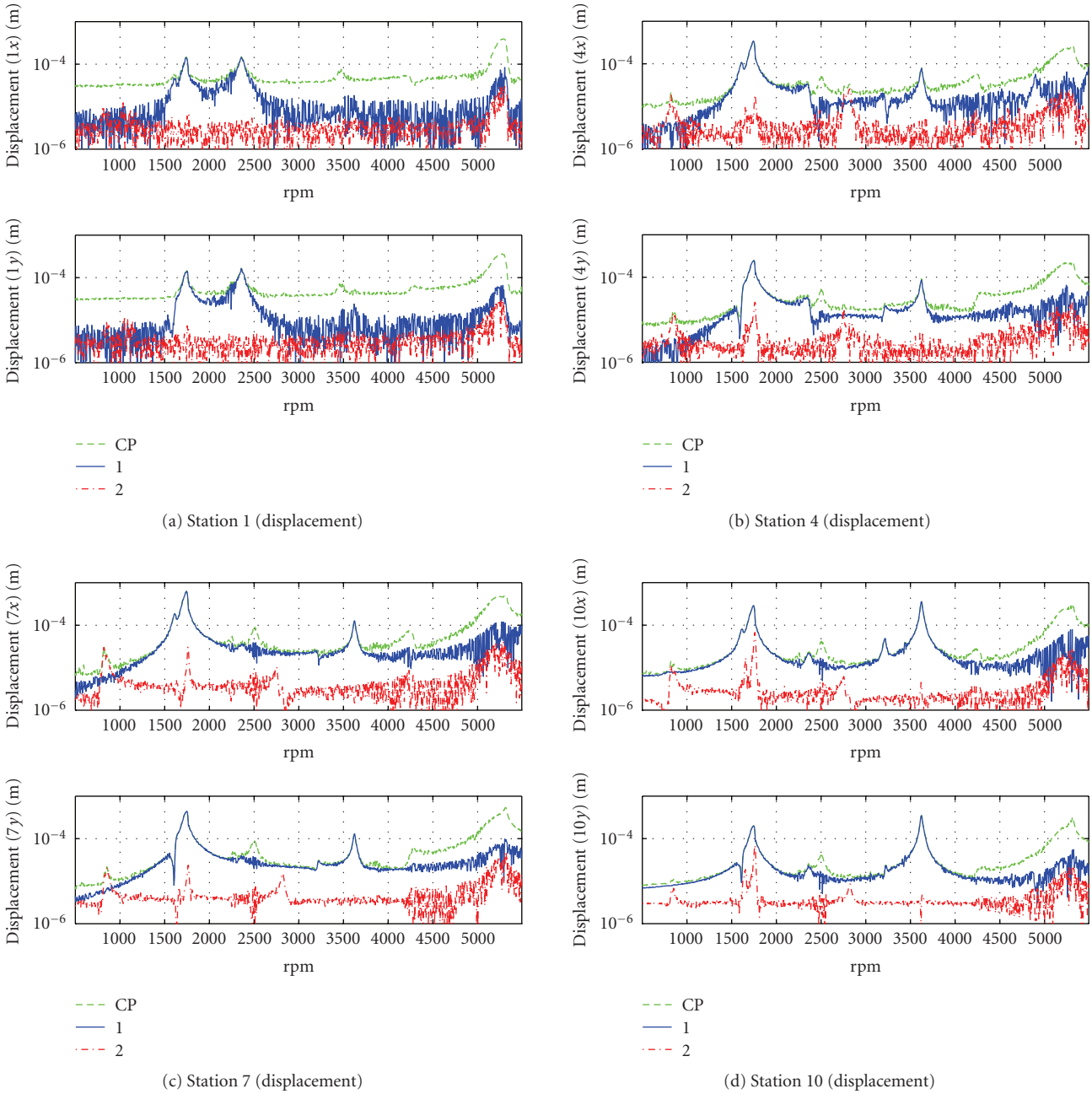

(a) Station 1 (displacement)

(b) Station 4 (displacement)

(c) Station 7 (displacement)

(d) Station 10 (displacement)

Figure 12: Order tracking measurements (rotor 2 reference, stations 1, 4, 7, and 10).

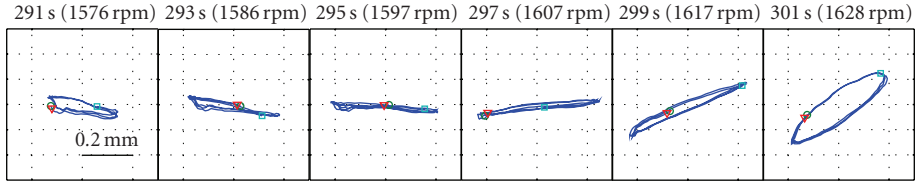

Figure 13: Orbits on the intershaft (measurement station 7) around the first backward whirl mode.

Table 3: Experimentally observed peaks.

N_1 (rpm)	N_2 (rpm)	*Order number* (rotor 1)	*Order number* (rotor 2)	*Interpretation*	*Deviation*
280	820	—	2	Mode 1 backward whirl	—
295	850	—	2	Mode 1 forward whirl	—
564	1615	—	1	Mode 1 backward whirl	7.7%
560	1655	—	2	Mode 3 backward whirl	—
610	1743	—	1	Mode 1 forward whirl	7.1%
608	1760	—	2	Mode 3 backward whirl	—
785	2255	2	—	Mode 1 backward whirl	—
830	2363	—	1	Mode 2 forward whirl	2.1%
875	2505	2	—	Mode 1 forward whirl	—
1138	3215	—	1	Mode 3 backward whirl	2.1%
1206	3450	2	—	Mode 2 forward whirl	—
1277	3623	—	1	Mode 3 forward whirl	0.1%
1495	4240	1	—	Mode 1 backward whirl	7.2%
1870	5300	1	—	Mode 1 forward whirl	7.1%

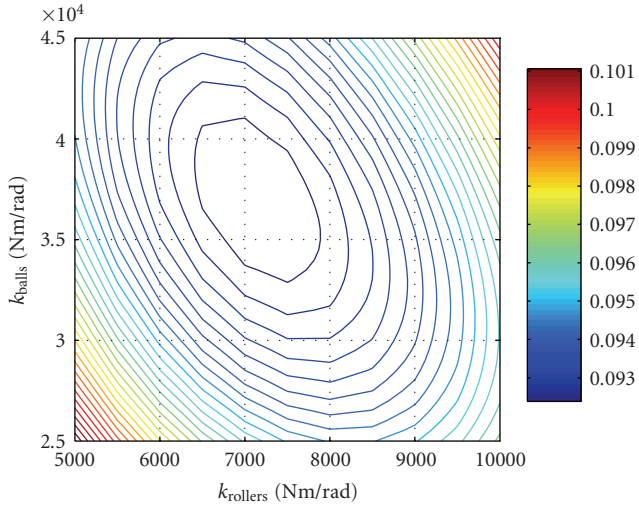

Figure 14: Quadratic error plot.

List of symbols

G: Gyroscopic matrix
K: Stiffness matrix
M: Mass matrix
R: Minimized error function
f: External forces vector
i: Imaginary unit
k: Stiffness coefficient
r: Intershaft bearing reaction
r: Minimized error function
v: Critical speed value
x: Generalized coordinates vector
η: Ratio between the rotation speed of the two rotors
λ: Sought eigenvalue
ω: Rotating speed

Superscripts

b: Beam element
d: Disk element
s: Spring element
1, 2: Matrix blocks splitting with respect to the intershaft coupling
exp: Experimental
quad: Quadratic deviation
th: Theoretical

Subscripts

balls: Corresponding to ball bearings
g: Gravity
rollers: Corresponding to roller bearings
1, 2: Rotor number
i: Critical speed value number.

ACKNOWLEDGMENT

The authors thank the Embassy of France in Russia for the financing of the mixed Ph.D. program between Ecole Centrale de Lyon and Bauman Moscow State Technical University.

REFERENCES

[1] T. A. Harris, *Rolling Bearing Analysis*, John Wiley & Sons, New York, NY, USA, 4th edition, 2001.
[2] F. E. Ehrich, *Handbook of Rotordynamics*, McGraw-Hill, New York, NY, USA, 1992.
[3] D. Childs, *Turbomachinery Rotordynamics: Phenomena, Modeling, and Analysis*, John Wiley & Sons, New York, NY, USA, 1993.
[4] J. M. Vance, *Rotordynamics of Turbomachinery*, John Wiley & Sons, New York, NY, USA, 1988.
[5] D. E. Bently, C. T. Hatch, and B. Grissom, *Fundamentals of Rotating Machinery Diagnostics*, Bently Pressurized Bearing Press, Minden, Nev, USA, 2002.

[6] S. Edwards, A. W. Lees, and M. I. Friswell, "Experimental identification of excitation and support parameters of a flexible rotor-bearings-foundation system from a single run-down," *Journal of Sound and Vibration*, vol. 232, no. 5, pp. 963–992, 2000.

[7] A. W. Lees and M. I. Friswell, "The evaluation of rotor imbalance in flexibly mounted machines," *Journal of Sound and Vibration*, vol. 208, no. 5, pp. 671–683, 1997.

[8] J. K. Sinha, A. W. Lees, and M. I. Friswell, "Estimating unbalance and misalignment of a flexible rotating machine from a single run-down," *Journal of Sound and Vibration*, vol. 272, no. 3–5, pp. 967–989, 2004.

[9] T. Yamamoto and Y. Ishida, *Linear and Nonlinear Rotordynamics: A Modern Treatment with Applications*, John Wiley & Sons, New York, NY, USA, 2001.

[10] J.-J. Sinou, C. Villa, and F. Thouverez, "Experimental and numerical investigations of a flexible rotor on flexible bearing supports," *International Journal of Rotating Machinery*, vol. 2005, no. 3, pp. 179–189, 2005.

[11] J. M. Vance and A. C. Royal, "High-speed rotor dynamics—an assessment of current technology for small turboshaft engines," *Journal of Aircraft*, vol. 12, no. 4, pp. 295–305, 1975.

[12] D. H. Hibner, "Dynamic response of viscous-damped multishaft jet engines," *Journal of Aircraft*, vol. 12, no. 4, pp. 305–312, 1975.

[13] K. Gupta, K. D. Gupta, and K. Athre, "Unbalance response of a dual rotor system. Theory and experiment," *Journal of Vibration and Acoustics*, vol. 115, no. 4, pp. 427–435, 1993.

[14] G. Ferraris, V. Maisonneuve, and M. Lalanne, "Prediction of the dynamic behavior of non-symmetric coaxial co- or counter-rotating rotors," *Journal of Sound and Vibration*, vol. 195, no. 4, pp. 649–666, 1996.

[15] H. D. Nelson and J. M. McVaugh, "The dynamics of rotor-bearing systems using finite elements," *ASME Journal of Engineering for Industry*, vol. 98, pp. 593–600, 1976.

[16] M. Lalanne and G. Ferraris, *Rotordynamics Prediction in Engineering*, John Wiley & Sons, New York, NY, USA, 2nd edition, 1990.